1993ApJ...403..164T

THE ASTROPHYSICAL JOURNAL, 403:164–174, 1993 January 20

WIGGLED STRUCTURE OF HERBIG-HARO OBJECTS: HELICAL KINK INSTABILITY OF JETS FROM YOUNG STELLAR OBJECTS

YASUSHI TODO
Theory and Computer Simulation Center, National Institute for Fusion Science, Chikusa-ku, Nagoya 464-01, Japan
YUTAKA UCHIDA
Department of Astronomy, Faculty of Science, University of Tokyo, Bunkyo-ku, Tokyo 113, Japan
TETSUYA SATO
Theory and Computer Simulation Center, National Institute for Fusion Science, Chikusa-ku, Nagoya 464-01, Japan
AND
ROBERT ROSNER
Department of Astronomy and Astrophysics, University of Chicago, Chicago, IL 60637
Received 1992 March 23; accepted 1992 July 28

ABSTRACT

We describe the results of three-dimensional magnetohydrodynamic numerical simulations, as applied to the behavior of the jets from young stellar objects (YSO jets) under circumstances in which the ambient large-scale interstellar magnetic field is twisted helically by the rotation of the protostar and the protostellar disk through which this field threads. The calculations are continued until the bow shock propagates a distance 60 times as far as the initial jet radius. The specific case we examine involves a jet with density $100m_H$ cm^{-3} and velocity 100 km s^{-1}; we then show that an azimuthal field B_ϕ of strength 70 μG drives a helical kink instability. The growth rate of this instability is large enough that significant morphological effects are expected to be visible during the typical lifetime of a HH object; for example, the observed "wiggled" appearance of some HH objects may be due to this helical kink instability.

Subject headings: ISM: jets and outflows — methods: numerical — MHD — stars: pre–main sequence

1. INTRODUCTION

Herbig-Haro objects (abbreviated "HH objects" in the following) are commonly found in the vicinity of young stellar objects (VSOs), and are characterized by their hydrogen Balmer-line emission and other emission lines, suggestive of shock heating (Schwartz 1975). HH objects are also commonly observed to be in rapid motion, as seen in their large proper motions away from the protostar, and in the high Doppler shifts seen in the above-mentioned lines. These motion indicators both suggest velocities in the range of 100–300 km s^{-1} (see review by Böhm 1989), although the exact values derived from these indicators for any one object differ from one another.

There exist four different scenarios for HH objects: (1) the "cavity focusing" model of Cantó (1980); (2) the "shocked cloudlet" model of Schwartz (1978); (3) the "interstellar bullet" model of Norman & Silk (1979); and (4) the "jet" model of Dyson (1984) and Mundt (1985). The purpose of this paper is to explore the nature of the last type of model in greater detail.

Recently, high-velocity (100–400 km s^{-1}) jets, called *YSO jets* or *optical jets*, were discovered yet closer to the forming stars, using CCD observations of star-forming regions (Mundt & Fried 1983). Although there is no apparent connection seen in general between YSO jets and HH objects, there are some observational clues suggesting a physical connection between YSO jets and HH objects. For example, HH 12 (Strom, Strom, & Stocke 1983; Strom et al. 1986) and HH 46/47 (Graham & Elias 1983; Meaburn & Dyson 1987; Reipurth & Heathcote 1991) show a filamentary structure connecting the source star and the bright HH object. This type of structure may imply an intrinsic relation between HH objects and YSO jets (Mundt et al. 1987), even though in more general cases such structures are not visible, Dyson (1984) and Mundt (1985) have indeed suggested relating such HH objects to the newly found YSO jets.

An essential point in attempting to relate HH objects to YSO jets is that these observations provide a number of constraints on any model. For example, one may ask why the shock strength as calculated from the ratios of emission lines is much lower than that inferred from the proper motion (emission spectrum/proper motion discrepancy; Raga 1989); how is their characteristic morphology, such as "jets with knots," or "wiggling filaments," formed; can the line-of-sight velocity field along its filamentary structure, and the proper motions of HH objects, be explained by the models thus far proposed?

In trying to resolve some of these problems, Uchida et al. (1992) proposed a new model in which YSO jets are guided along an ambient large-scale magnetic field, which has itself been twisted in the process of star formation; these jets then produce a bow shock, a jet-terminal shock, and two slow shocks. Within the context of such a model, cases such as HH 12 or HH 46/47 are viewed as special instances in which the structure connecting these HH objects with the related YSOs happens to be made visible by the pinch effect of the helical magnetic field; in most other cases, the connecting structure may not be visible because of a lateral expansion of the background magnetic field (so that only the parts heated by the shocks are visible). Todo et al. (1992) has performed 2.5 dimensional MHD simulations appropriate to this physical setting, and has pointed out that HH 47A and HH 47D can be interpreted as a single jet in a strong magnetic field, rather than two arbitrarily assumed successive events within a nonmagnetic medium. They also suggested that the wiggled filaments of HH 12 and HH 46/47, as well as of HH 33/40 (Mundt, Brugel, & Bührke 1987) and HH 110 (Reipurth 1989), may be the result of an MHD helical kink instability. In this paper, we use the tools of MHD simulations to further explore this model, focusing in particular on the dynamics of the YSO jet in the presence of an ambient large-scale background magnetic field.

In order to guide our discussion about the models, we begin by describing the physical picture of the star-forming region we have in mind. We suppose that we have a situation in which a protostellar disk has formed perpendicularly to the original large-scale magnetic field which initially pervaded the star-forming region. This kind of disk orientation may be the result of an initial rapid loss of the angular momentum components perpendicular to the field (viz., through the generation of Alfvén mode disturbances by the collapsing cloud; see, e.g., Mestel 1965). It has been further argued that the parallel component of angular momentum is lost toward the final phase through magnetic braking (Mouschovias & Paleologou 1979). Uchida & Shibata (1985) have noted that this process necessarily creates an azimuthal component of the magnetic field in the differentially rotating disk, and that as a result, nonlinear torsional Alfvén waves propagate along the large-scale magnetic field. The azimuthal magnetic field associated with these nonlinear torsional Alfvén waves can pinch the poloidal magnetic field, as well as the ambient medium in which it is embedded, and as a result, both the poloidal and toroidal components of the large-scale magnetic field can become much stronger than the magnetic field in the undisturbed background interstellar medium. It is in this context, after the protostar has formed, that we suppose a YSO jet may be "guided" by this preexisting large-scale magnetic field, so that the direction of the jet is parallel to the axis of the large-scale helical field.

In the present paper, we analyze the behavior of these YSO jets, focusing on the suggestion (by Todo et al. 1992) that these jets may be subject to an MHD helical kink instability, and thereby attain a helical form. Our analysis makes use of fully three-dimensional MHD simulations in order to explore jet dynamics which can lead to such geometric distortions. Thus, we note that although a number of other (hydrodynamical and MHD) jet simulations in a similar physical context have been performed (see, e.g., Norman et al. 1982; Clarke, Norman, & Burns 1986; Lind et al. 1989; Kössl, Müller, & Hillebrandt 1990), these have been limited to the two-dimensional situation, and further have all assumed that no large-scale ambient poloidal magnetic field is present. We shall relax both assumptions and focus on the behavior of nonaxisymmetric modes in our three-dimensional simulations.

We structure our paper as follows: in § 2, we describe the system of equations, the initial and boundary conditions, and the numerical method for our MHD jet simulations. The results of our simulations are presented in § 3. The physical properties of the jets derived from our simulations, and the astrophysical implications of our results, are discussed in § 4; we summarize our results in § 5.

2. EQUATIONS, INITIAL AND BOUNDARY CONDITIONS, AND NUMERICAL METHOD

We use the standard system of three-dimensional ideal MHD equations, written using a cylindrical coordinate system (r, ϕ, z),

$$\frac{\partial \rho}{\partial t} = -\frac{1}{r}\frac{\partial}{\partial r}(r\rho v_r) - \frac{\partial}{r\,\partial \phi}(\rho v_\phi) - \frac{\partial}{\partial z}(\rho v_z)\,, \tag{1}$$

$$\begin{aligned}\frac{\partial}{\partial t}(\rho v_r) = &-\frac{\partial p_{\rm total}}{\partial r} - \frac{1}{r}\frac{\partial}{\partial r}\left(r\rho v_r^2 - r\frac{B_r^2}{\mu_0}\right) \\ &- \frac{\partial}{r\,\partial\phi}\left(\rho v_r v_\phi - \frac{B_r B_\phi}{\mu_0}\right) - \frac{\partial}{\partial z}\left(\rho v_r v_z - \frac{B_r B_z}{\mu_0}\right) \\ &+ \frac{\rho v_\phi^2}{r} - \frac{B_\phi^2}{\mu_0 r}\,,\end{aligned} \tag{2}$$

$$\begin{aligned}\frac{\partial}{\partial t}(\rho v_\phi) = &-\frac{\partial p_{\rm total}}{r\,\partial \phi} - \frac{1}{r}\frac{\partial}{\partial r}\left(r\rho v_r v_\phi - r\frac{B_r B_\phi}{\mu_0}\right) \\ &- \frac{\partial}{r\,\partial\phi}\left(\rho v_\phi^2 - \frac{B_\phi^2}{\mu_0}\right) - \frac{\partial}{\partial z}\left(\rho v_\phi v_z - \frac{B_\phi B_z}{\mu_0}\right) \\ &- \frac{\rho v_r v_\phi}{r} + \frac{B_r B_\phi}{\mu_0 r}\,,\end{aligned} \tag{3}$$

$$\begin{aligned}\frac{\partial}{\partial t}(\rho v_z) = &-\frac{\partial p_{\rm total}}{\partial z} - \frac{1}{r}\frac{\partial}{\partial r}\left(r\rho v_r v_z - r\frac{B_r B_z}{\mu_0}\right) \\ &- \frac{\partial}{r\partial\phi}\left(\rho v_\phi v_z - \frac{B_\phi B_z}{\mu_0}\right) - \frac{\partial}{\partial z}\left(\rho v_z^2 - \frac{B_z^2}{\mu_0}\right),\end{aligned} \tag{4}$$

$$\frac{\partial B_r}{\partial t} = \frac{\partial}{r\,\partial\phi}(v_r B_\phi - v_\phi B_r) - \frac{\partial}{\partial z}(v_z B_r - v_r B_z)\,, \tag{5}$$

$$\frac{\partial B_\phi}{\partial t} = \frac{\partial}{\partial z}(v_\phi B_z - v_z B_\phi) - \frac{\partial}{\partial r}(v_r B_\phi - v_\phi B_r)\,, \tag{6}$$

$$\frac{\partial B_z}{\partial t} = \frac{1}{r}\frac{\partial}{\partial r}(r v_z B_r - r v_r B_z) - \frac{\partial}{r\,\partial\phi}(v_\phi B_z - v_z B_\phi)\,, \tag{7}$$

$$\begin{aligned}\frac{\partial E}{\partial t} = &-\frac{1}{r}\frac{\partial}{\partial r}[r(E + p_{\rm total})v_r - rFB_r] \\ &- \frac{\partial}{r\,\partial\phi}[(E + p_{\rm total})v_\phi - FB_\phi] - \frac{\partial}{\partial z}[(E + p_{\rm total})v_z - FB_z]\,,\end{aligned} \tag{8}$$

where

$$E = \frac{1}{2}\rho \boldsymbol{v}^2 + \frac{1}{\gamma - 1}p + \frac{\boldsymbol{B}^2}{2\mu_0}\,, \tag{9}$$

$$F = \frac{\boldsymbol{B}\cdot\boldsymbol{v}}{\mu_0}\,, \tag{10}$$

$$p_{\rm total} = p + \frac{\boldsymbol{B}^2}{2\mu_0}\,. \tag{11}$$

Here μ_0 is the vacuum permeability and γ is the adiabatic constant, and all other quantities have their customary meaning. These nonlinear equations are solved by numerical methods, as described in detail below.

The initial physical state of our simulation can be described as follows. We assume constant pressure, a force-free helical magnetic field, and collimated jet injection. We place a higher density region in the eventual path of the jet in order to examine the effects of an encounter of a jet with an interstellar mass clump. The physical properties of the jet are characterized as follows: we define R, V_j, and ρ_j as the radius, the velocity, and the density, respectively, of the jet as it is injected into the computational domain. These quantities will be used below in order to non-dimensionalize (and scale) the length, velocity, and density scales, respectively, of our problem. In the context of YSO jets, the velocity and density of the jets are known to be of the order 100 km s^{-1} and $100 m_{\mathrm{H}}\ \mathrm{cm}^{-3}$, respectively.

We further assume that the initial state can be characterized as follows:

$$\rho = \rho_j f(r, z) + \rho_{\mathrm{amb}}[1 - f(r, z)] + (\rho_{\mathrm{clump}} - \rho_{\mathrm{amb}}) g(r, z) , \tag{12}$$

$$p = p_0 = \mathrm{const} , \tag{13}$$

$$v_r = 0 , \tag{14}$$

$$v_\phi = 0 , \tag{15}$$

$$v_z = V_j f(r, z) , \tag{16}$$

$$f(r, z) = \frac{1}{2}\left\{1 + \tanh\left[\frac{(z_j - z)}{w_z}\right]\right\}\left\{1 + \tanh\left[\frac{(R^2 - r^2)}{(w_r^2 + 2Rw_r)}\right]\right\} \times \left\{1 + \tanh\left[\frac{R^2}{(w_r^2 + 2Rw_r)}\right]\right\}^{-1} , \tag{17}$$

$$g(r, z) = \frac{1}{2}\left\{1 + \tanh\left[\frac{(z - z_1)}{w_z}\right]\right\}\left\{1 + \tanh\left[\frac{(z_2 - z)}{w_z}\right]\right\} , \tag{18}$$

where ρ_{amb} is the density of the ambient interstellar medium, ρ_{clump} is the density of the high-density region in the interstellar medium, z_j is the z-coordinate of the top of the jet at $t = 0$ measured from the bottom boundary of the simulation, z_1 and z_2 are the z-coordinates at the edges of the clump, and w_z and w_r are the widths of the transitions on the jet surface in the density and the velocity field in the r- and z-direction, respectively. The geometric "shape functions" are scaled as follows: $f(r, z)$ and $g(r, z)$ are defined such that $f(r, z) = 1$ inside the jet ($r \lesssim R$, $z \lesssim z_j$) and $f(z, r) = 0$ outside the jet, and $g(r, z) = 1$ ($z_1 \lesssim z \lesssim z_2$) and $g(r, z) = 0$ ($z \lesssim z_1$, $z \gtrsim z_2$), respectively; w_r and w_z are taken to be 0.21 R and 0.4 R, respectively; z_j, z_1, and z_2 are taken to be 0, 15 R, and 20 R, respectively; p_0 is chosen such that $M = V_j/(\gamma p_0/\rho_j)^{1/2}$, where M is the hydrodynamical Mach number inside the jet.

The initial magnetic field is assumed for simplicity to be a helical force-free field, which is uniform in the z-direction and has no radial component; it is explicitly given by

$$B_r = 0 , \tag{19}$$

$$B_\phi = B_0\left[\frac{0.5A\, dr^2}{(r + 0.5d)^3}\right]^{0.5} , \tag{20}$$

$$B_z = B_0\left[\frac{1 - Ar^2(r + d)}{(r + 0.5d)^3}\right]^{0.5} , \tag{21}$$

where B_0 is the magnetic field strength on the axis, the factor A scales the azimuthal field strength in terms of B_0, and the maximum B_ϕ is given by $0.385 B_0 (A)^{1/2}$ at $r = d$. B_0 is chosen such that $M_{\mathrm{A}} = V_j/(B_0^2/\mu_0 \rho_j)^{1/2}$, where M_{A} is the Alfvén Mach number inside the jet. Although we have no particular observational grounds for the particular functional form assumed for B_ϕ, we do note that $B_\phi \propto r$ ($r \sim 0$) and $B_\phi \propto r^{-0.5}$ ($r \sim \infty$) for plausible rotation curves for the system consisting of the protostar and the protostellar disk; thus, the chosen functional form has some physical plausibility. We have assumed $A = 0.99$ and $d = 3 R$.

The total simulation region is taken to be $0 \le r \le 60\ R$, $-63\ R \le z \le 63\ R$ for $z_j = 0$, although the region of our direct concern is $0 < z < 60\ R$ and $r < 5\ R$. The size of the region behind the top of the jet at $t = 0$ ($z < 0$) and the large width in r are both chosen so as to minimize the effects of reflection from the boundaries of disturbances caused by the high-velocity jet. This condition, together with the free boundary conditions described below, do satisfactorily suppress boundary effects. As for the grid point spacing used in the calculation, we assign fewer grid points in the region far away from the jet by smoothly varying the grid intervals in the r- and z-directions towards the outer boundaries. The numbers of the grid points used in our runs are $(N_r, N_\phi, N_z) = (105, 12, 138)$, of which (65, 12, 105) are assigned to the region of our main concern, and the rest are distributed in the marginal region outside.

The boundary conditions at $r = 60\ R$ are "free boundary conditions" for disturbances, i.e., the increments of all physical quantities are set equal to the ones at the grid points just inside of the boundary grid points. For example,

$$\rho_i^{n+1} = \rho_i^n + (\rho_{i-1}^{n+1} - \rho_{i-1}^n) , \tag{22}$$

where i and $i - 1$ are the indices of the grid points, and n and $n + 1$ are the indices of the time steps. At the other boundaries ($z = -63\ R$ and $z = 63\ R$), all physical quantities are fixed at the initial value.

The numerical scheme used to advance the above set of time-dependent, three-dimensional MHD equations was developed from a TVD scheme proposed by Roe (1981), and applied to MHD by Brio & Wu (1988). Roe's scheme is an upwind scheme applied to hyperbolic problems. In each computational cell, the problem is linearized around some average state, so that the flux difference is preserved in each cell. This linear system is decomposed into a set of uncoupled scalar linear equations. We have improved the scheme so that it is now of second-order accuracy in space and time by adopting the MUSCL method (van Leer 1979) and by introducing two-step time integration. Because we basically assume independence of the three spatial directions r, ϕ, and z, $\operatorname{div} \boldsymbol{B} = 0$ is not necessarily automatically satisfied. In order to maintain $\operatorname{div} \boldsymbol{B}$ at very small values, we introduce a particular type of artificial diffusion in the magnetic field evolution equation at each time step such that

$$\boldsymbol{B}^{\mathrm{new}} = \boldsymbol{B} + \nu \operatorname{grad} \operatorname{div} \boldsymbol{B} \Delta t , \tag{23}$$

where ν is a constant and Δt is the duration of each time step. For the present calculations, ν is set to $\nu = 0.2 \Delta x V_j$, where Δx is the smallest grid spacing in the r-direction (which in our case is 0.075 R). Since in our simulations the largest deviation of $\operatorname{div} \boldsymbol{B}$ is a few times $0.01 |\boldsymbol{B}|/\Delta x$, the additional term brings about at most a few times 0.1% change in the magnetic field. The logic underlying our use of this type of artificial diffusivity is that we add a bulk viscosity to the magnetic field in order to suppress the growth of the divergence of the field. As a test of our procedures, we have compared results obtained with our modified code against solutions of the one-dimensional MHD Riemann problem of Brio & Wu (1988) and the two-dimensional solar coronal transient solution of Low (1984). For the one-dimensional Riemann problem, we obtained the same results as Brio & Wu; for Low's solution, we used a 100 × 100 grid, and our results coincide closely with the analytical theory. For example, we have reproduced the propagation velocity of the shock wave and the maximum fluid velocity within 0.7% and 1.3%, respectively. The results of these tests are described and discussed in Todo (1991).

We now apply a nonaxisymmetric perturbation to the initial magnetic field alone (i.e., no perturbations are applied to any of the other physical quantities), as follows:

$$\xi_\phi = Ce^{i(m\phi + kz)}\left(-\frac{kr}{m} + i\frac{r}{m}\frac{\partial}{\partial z}\right)h(z)\,, \tag{24}$$

$$\xi_z = Ch(z)e^{i(m\phi + kz)}\,, \tag{25}$$

$$b_r = 0\,, \tag{26}$$

$$b_\phi = \frac{\partial}{\partial z}(\xi_\phi B_z - \xi_z B_\phi)\,, \tag{27}$$

$$b_z = -\frac{\partial}{r\,\partial\phi}(\xi_\phi B_z - \xi_z B_\phi)\,, \tag{28}$$

where

$$h(z) = \frac{1}{4}\left\{1 + \tanh\left[\frac{(z - z_3)}{w_p}\right]\right\}\left\{1 + \tanh\left[\frac{(z_4 - z)}{w_p}\right]\right\}. \tag{29}$$

This perturbation is assumed to be localized around the contact surface of the tip of the jet and the ambient medium (i.e., at $z = 0$); $z_3 = -5\ R$, $z_4 = 5\ R$, and $w_p = 2\ R$. We set $m = 1$, $k = -2\pi/\lambda$, $\lambda = 20\ R$, and C is a constant which is chosen such that the maximum value of $|\boldsymbol{b}|/|\boldsymbol{B}|$ is 0.01 in the present study. Note that an axisymmetric helical magnetic field which has positive helicity ($B_z B_\phi > 0$) is more unstable for $mk < 0$ perturbations than for $mk > 0$, because $mk < 0$ perturbations have a helical structure such that they untwist the helical magnetic field, and thus liberate its free energy.

3. RESULTS OF SIMULATIONS

As an illustration, and demonstration, of the physics which underlies the evolution of a jet under the conditions described above, we shall now investigate a specific case, with $M = 6$ and $M_{\rm A} = 2.5$. The maximum value of B_ϕ, which is defined in equation (20), is $\sim 0.15(\mu_0 \rho_j)^{1/2} V_j$. For a jet with $\rho_j = 100 m_{\rm H}$ and $V_j = 100$ km s^{-1}, this Alfvén Mach number means that B_0 (magnetic field strength on the z-axis) and the maximum B_ϕ are set to be 182 and 70 μG, respectively. Since this calculation focuses on the dynamics of the problem, we will not introduce the energy-loss term in the energy equation; furthermore, since the dominant internal energetics is most likely cooling by radiation, we will assume that $\gamma = 1.2$. At the initial stage, a sheetlike clump with higher-than-ambient density is placed ahead of the jet, and $\rho_{\rm amb}$ and $\rho_{\rm clump}$ are set to be ρ_j and 10 ρ_j, respectively. Our initial case is thus the same as case MH4 of Todo et al. (1992), with the exception that a clump is placed ahead of the jet; in addition, we now solve the full three-dimensional case. This model situation also resembles the case treated by Uchida et al. (1992) via a 1.5 dimensional simulation.

3.1. *Appearance of Shocks*

We first show an early stage ($t = 20\ R/V_j$) of our simulation in a projection on the $r - z$ plane ($\phi = 0, \pi$) in Figure 1. As pointed out by Todo et al. and Uchida et al., four shocks are formed; these are a fast-mode, a slow-mode, a slow-mode, and a fast-mode shock, respectively, when counting from the front of the jet. The forward fast-mode shock is the bow shock. B_ϕ and v_ϕ are strong behind each fast-mode shock, whereas the thermal pressure is strong between the two slow shocks. The jet medium, heated up by the fast-mode and slow-mode shocks, expands laterally, thereby stretching the magnetic field and forming a cocoon. B_ϕ takes its maximum value behind the backward fast-mode shock; the maximum value of B_ϕ is $0.45 B_0$, which is 2.9 times higher than the maximum value of B_ϕ in the initial state.

3.2. *Collision with a Clump*

At $t = 40\ R/V_j$, the forward fast-mode shock has encountered the sheetlike clump (Fig. 2). After the encounter of the forward fast-mode shock with the clump, a reflection wave propagates backward and enhances the B_ϕ strength. The maximum value of B_ϕ is $0.78 B_0$, which is 4.7 times higher than the maximum value of B_ϕ in the initial state, and 1.7 times higher than that at $t = 20\ R/V_j$. This stronger B_ϕ drives a helical kink instability more rapidly, as will be discussed below. The interactions of the reflected shock waves are the same—in a qualitative sense—as the results of Uchida et al. (1992).

3.3. *Helical Kink Instability*

At the final stage of our calculation ($t = 128\ R/V_j$), a helical kink instability has taken place and has grown to a nonlinear stage behind the backward fast-mode shock (Fig. 3). We note that contours of both the density and pressure show a sine-curve structure in the $r - z$ plane, which can be readily interpreted as a projection of an actual helical structure in three-dimensional space. The poloidal magnetic field (B_r, B_z) also shows a structure consistent with that of the density and pressure.

How can we be sure that we are actually looking at a magnetohydrodynamic helical kink instability? In Figure 4*c* we show the spatial distribution of $(-v_r j_z B_\phi)$, which is the work done by the $(-j_z B_\phi)$ force per unit time on the $r - z$ plane ($\phi = 0, \pi$) at $t = 110\ R/V_j$, where j_z is defined as

$$j_z = \frac{1}{\mu_0}\left(\frac{\partial}{r\,\partial r} r B_\phi - \frac{\partial}{r\,\partial\phi} B_r\right). \tag{30}$$

A correlation between the sine-curve (i.e., helical in three-dimensional space) structure of the density field and the work term $(-v_r j_z B_\phi)$ is clearly seen. The correlation is consistent with the idea that the helical structure is formed by the $(-j_z B_\phi)$ force.

We further show the magnetic field lines at $t = 0$ and $t = 120\ R/V_j$ in Figure 5. The internal twist of the magnetic field relaxes in the region where the instability has taken place, and a large-scale twist is formed. This internal untwisting of the field is a characteristic feature of the helical kink instability and provides yet further support for our interpretation of the dynamics, and for our model. Furthermore, the large-scale twist is a right-hand helix; that is, the large-scale twist has a positive helicity. Because the total magnetic helicity is conserved, this large-scale helicity must be simply the result of the up-conversion of small-scale "internal" helicity located initially within the jet, which unwinds itself in the process of the helical kink instability. This characteristic implies that astrophysical jets which are bent due to the helical kink instability would tend to have magnetic fields parallel to the wiggled structure (this tendency would not be conspicuous in objects at an unsaturated stage of the instability).

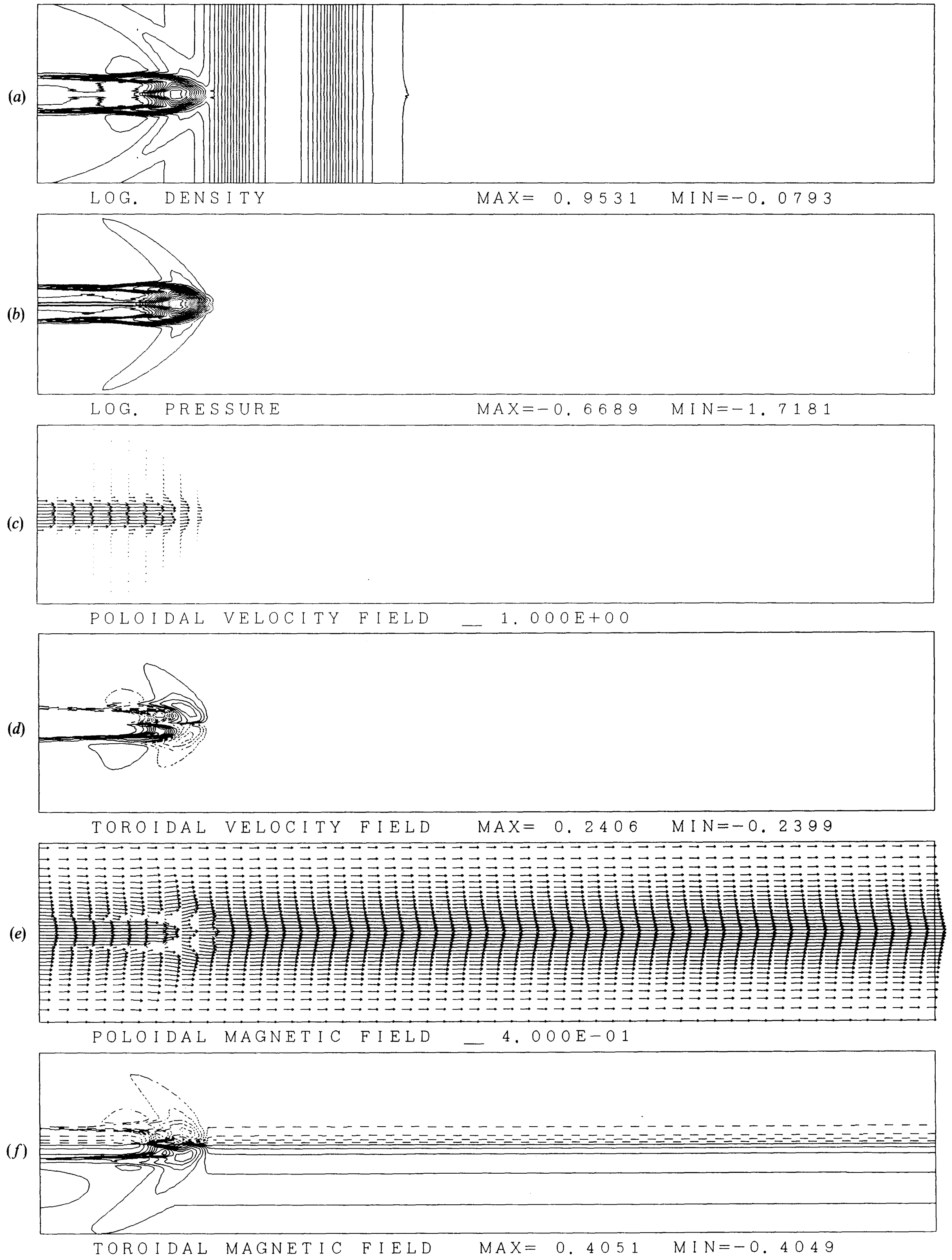

FIG. 1.—(*a*) Contours of log ρ; (*b*) contours of log p; (*c*) poloidal velocity vector $\boldsymbol{v}_p = (v_r, v_z)$; (*d*) contours of v_ϕ; (*e*) poloidal magnetic field vector $\boldsymbol{B}_p = (B_r, B_z)$; (*f*) contours of B_ϕ, at $t = 20\ R/V_j$ on a $r - z$ plane ($\phi = 0, \pi$). In (*d*) and (*f*), solid curves correspond to a direction from the front side to the reverse side of the paper, whereas dashed curves correspond to the opposite direction. Behind forward and backward fast-mode shocks, the density, pressure and B_ϕ are all strengthened; in contrast, a weak B_ϕ, but high density and pressure, appears behind the two slow-mode shocks.

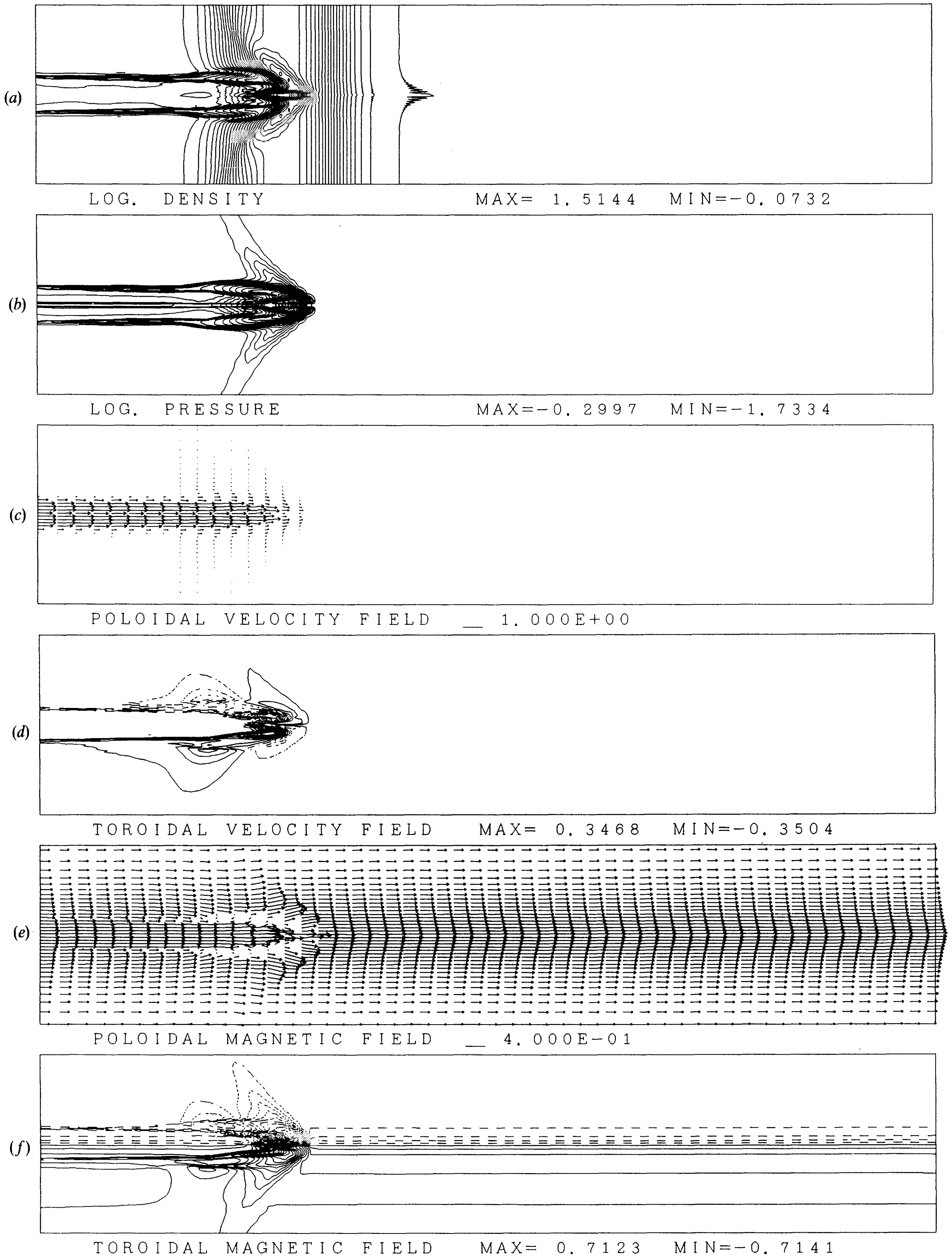

FIG. 2.—(*a*) Contours of log ρ; (*b*) contours of log p; (*c*) poloidal velocity vector $\boldsymbol{v}_p = (v_r, v_z)$; (*d*) contours of v_ϕ; (*e*) poloidal magnetic field vector $\boldsymbol{B}_p = (B_r, B_z)$; (*f*) contours of B_ϕ, at $t = 40\ R/V_j$ on the $r - z$ plane ($\phi = 0, \pi$). In (*d*) and (*f*), solid curves correspond to a direction from the front side to the reverse side of the paper, whereas dashed curves correspond to the opposite direction. B_ϕ becomes stronger than in Fig. 1 due to intense compression caused by the collision between the jet and the heavy clump.

1993ApJ...403..164T

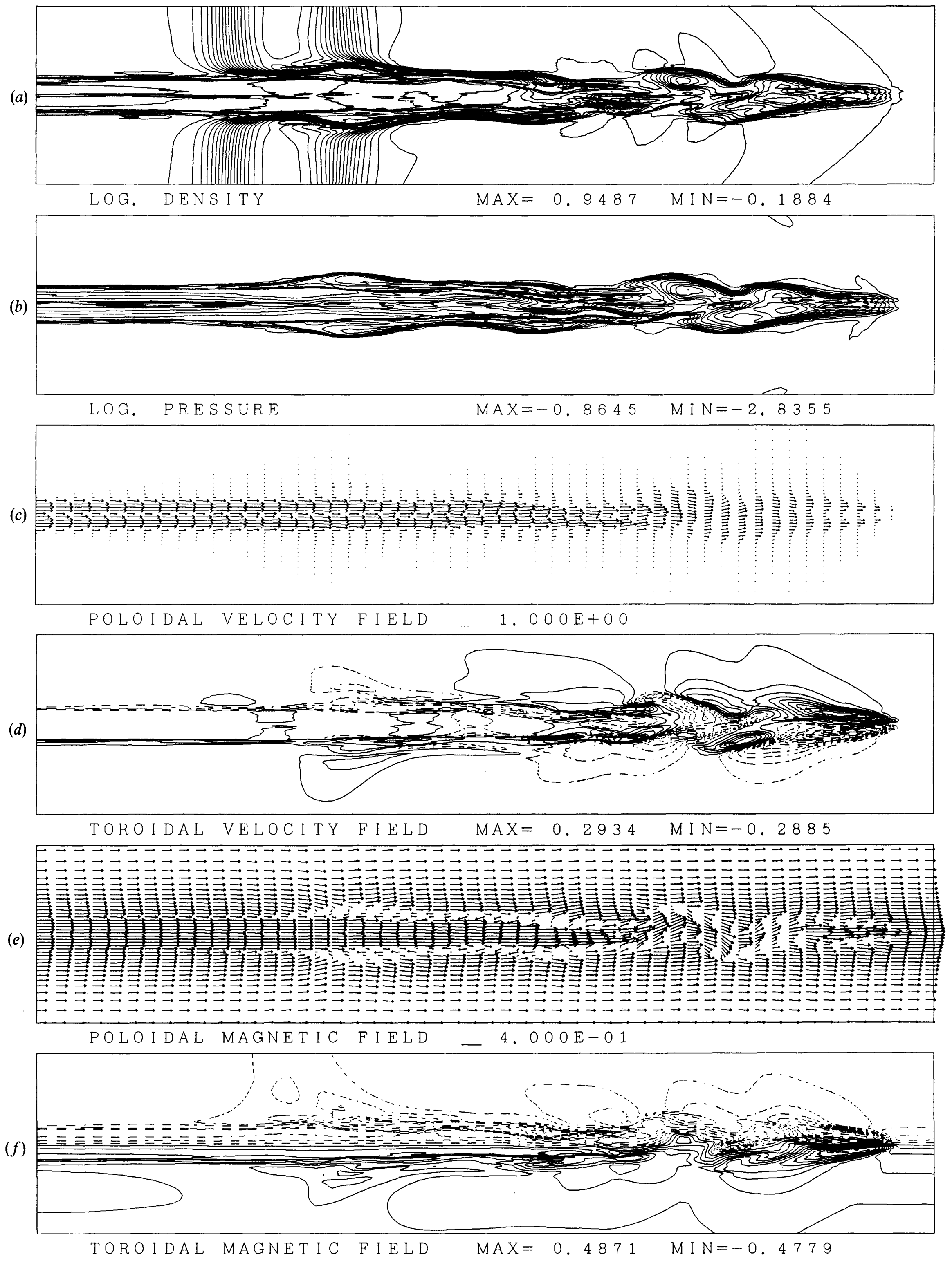

FIG. 3.—(*a*) Contours of log ρ; (*b*) contours of log p; (*c*) poloidal velocity vector $\boldsymbol{v}_p = (v_r, v_z)$; (*d*) contours of v_ϕ; (*e*) poloidal magnetic field vector $\boldsymbol{B}_p = (B_r, B_z)$; (*f*) contours of B_ϕ, at $t = 128R/V_j$ on a $r - z$ plane ($\phi = 0, \pi$). In (*d*) and (*f*), solid curves correspond to a direction from the front side to the reverse side of the paper, whereas dashed curves correspond to the opposite direction. Helical kink instability takes place, and forms a helical structure. The v_ϕ field shows that the gas flows along the helical structure.

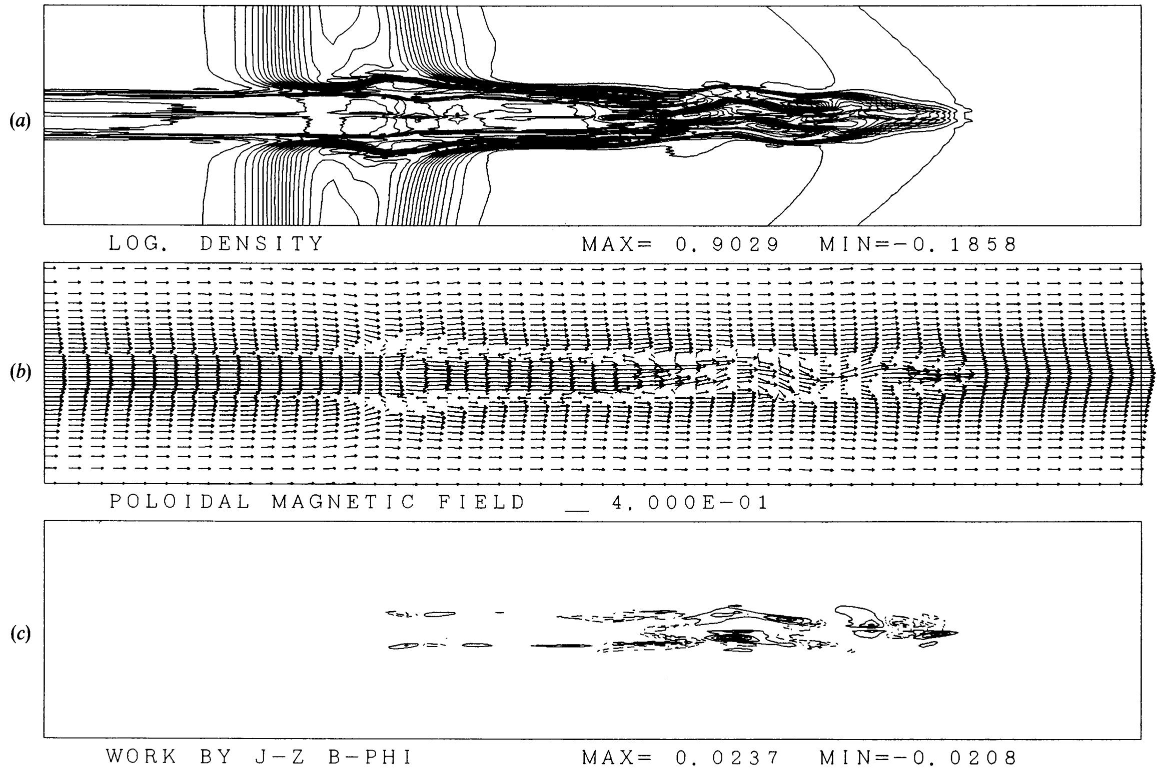

FIG. 4.—(*a*) Contours of log ρ; (*b*) poloidal magnetic field vector $\boldsymbol{B} = (B_r, B_z)$; (*c*) contours of $(-v_r j_z B_\phi)$, of a magnetohydrodynamic jet at $t = 110\,R/V_j$ on the $r - z$ plane ($\phi = 0, \pi$). In (*c*) solid curves correspond to the positive work done by the $(-j_z B_\phi)$ force per unit time, whereas dashed curves correspond to the negative work. The observed correlation between density and $(-v_r j_z B_\phi)$ in the helically deformed region suggests that the driving force of this instability is $(-j_z B_\phi)$.

Our final argument identifying the instability observed in our results with the MHD kink mode compares our simulation results with the expected behavior of the $m = 1$ mode, and in particular with the temporal growth of the $m = 1$ mode, as well as its dependence on wavelength. Thus, consider in Figure 6 the Fourier coefficient of the magnetic energy spectrum, which is defined as follows:

$$I(\lambda) = \frac{|P(\lambda)|}{P_{\text{total}}}\,, \tag{31}$$

where

$$P(\lambda) = \int_0^{60R} dz \int_0^{2\pi} d\phi \int_0^{2R} \frac{\boldsymbol{B}^2}{2\mu_0}\, e^{i(\phi - 2\pi z/\lambda)} r\, dr\,, \tag{32}$$

$$P_{\text{total}} = \int_0^{60R} dz \int_0^{2\pi} d\phi \int_0^{2R} \frac{\boldsymbol{B}^2}{2\mu_0}\, r\, dr\,. \tag{33}$$

The maximum growth rate is $\sim 0.06 V_j/R$ (the minimum *e*-folding time is $\sim 17\,R/V_j$) at a wavelength of $\sim 18\,R$, as seen in Figure 6*b*.

Next we compare this result with that of the well-known sheath current approximation model (Shafranov 1957; Kruskal et al. 1958). The sheath current approximation treats a plasma column of infinite length, which is confined by an external magnetic field in vacuum; we further assume that the pressure density and B_z are uniform, and that the value of B_z is B_{iz} in a static plasma. The external magnetic field has a constant *z*-component $B_z = B_{ez}$, and B_ϕ. (The latter's source is the sheath current in the *z*-direction on the surface of the plasma column.) The critical wavelength and the growth rate in the $B_{ez} \gg B_\phi$ limit are given as follows:

$$\lambda_{\text{cr KS}} = \frac{2\pi R B_z}{B_\phi}\,, \tag{34}$$

$$\mu_0 \rho w^2 = k^2 B_{iz}^2 + \left(k B_{ez} + \frac{m}{R} B_\phi\right)^2 - \frac{m}{R^2} B_\phi^2\,, \tag{35}$$

where $k = 2\pi/\lambda$, ω is the frequency in the linear analysis, and Im ω is the growth rate. In order to compare the results of the sheath current approximation model with those of our simulation, we estimate the growth rate from equation (35) for the values of B_z, B_ϕ, and ρ taken to the maximum values of those in our results. From Figure 1, $B_{iz} \sim B_{ez} \sim B_0$, $B_\phi \sim B_0$, and $\rho \sim 4\rho_j$, so that we have Im $\omega_{\lambda = 18R} \sim 0.13 V_j/R$. This growth rate coincides with the rate deduced from the results of our simulation mentioned above within a factor of 2.2.

Of course, this sheath current approximation must be somewhat cautiously compared with our simulation results because it neglects the nonuniformity in both the *r*- and *z*-directions, as well as the flow, which we have taken into account in our calculations. Nevertheless, we believe that the agreement between the simulation and the simple linear theory provides further support for the suggestion that the helical structure is formed by the helical kink instability rather than by other processes.

3.4. *The* v_ϕ *Field*

In Figure 3*d* ($t = 128\,R/V_j$), v_ϕ appears to have a different geometric structure from that seen in Figure 1*d* ($t = 20\,R/V_j$).

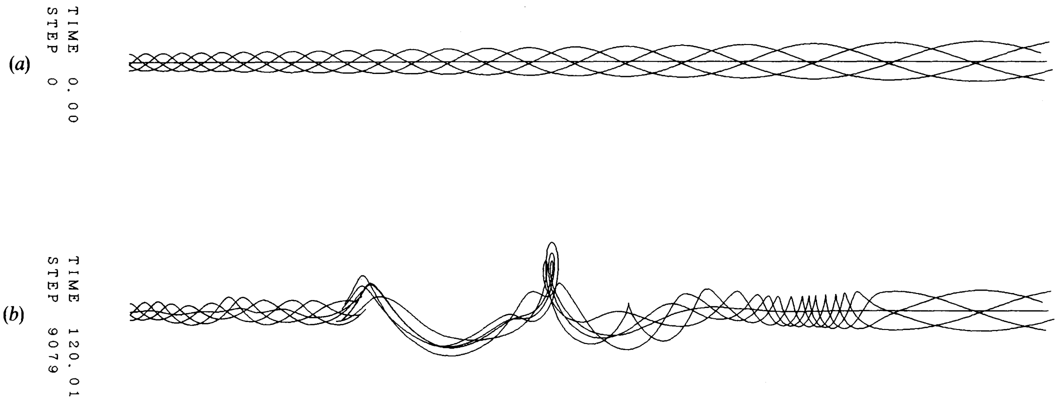

FIG. 5.—Magnetic field lines whose footpoints are on the z-axis and at 0.2 R from the z-axis at (*a*) $t = 0$ and (*b*) $t = 120 R/V_j$ in $0 < z < 60\ R$. Lines are integrated along the magnetic field both from the top and the bottom in (*b*). All lines are projected from a viewpoint located at $r = 34\ R$, $\phi = 0$, $z = 94\ R$ onto a plane which is normal to the line which connects the origin to the viewpoint and has the origin on it. The figure is compressed 0.4 times in the z-direction. A large-scale helix is formed at $t = 120\ R/V_j$. Note that in the helically deformed region, the internal twist relaxes. This internal untwisting is a characteristic of the helical kink instability.

In the region where the form of the jet is distorted leftward (i.e., in the "$-r$"-direction in the $r - z$ plane), v_ϕ tends to become negative (in the direction from the backside of the paper and toward the reader), whereas in the rightward-distorted region, v_ϕ tends to become positive. If we trace this velocity field, we obtain a right-hand helical velocity field. As mentioned in § 3.3 above, the magnetic lines of force in the helical structure form a right-hand helix in three-dimensional space. This form for the v_ϕ field means that the gas has begun to flow *along* the helical structure. Furthermore, the v_ϕ field in Figure 1*d* shows evidence for an internal spinning motion initially, while in Figure 3*d*, the velocity field of the flow along the large-scale helical structure clearly overwhelms that of the internal spinning motion.

4. DISCUSSION

4.1. *Comparison of Geometric Structures of HH 46/47 and Simulation Results*

We have already several times noted the remarkable geometric similarity between our model results and the observed structure of HH 46/47. Todo et al. (1992) have pointed out in their analysis of 2.5 dimensional simulations that HH 47D can be interpreted as a forward-propagating fast-mode shock (i.e., as a bow-shock type of object), and that the region between the two slow-mode shocks may then well correspond to HH 47A; this interpretation follows from our results as well. We have further shown above that the helical filament is readily interpreted as having been formed by a helical kink instability.

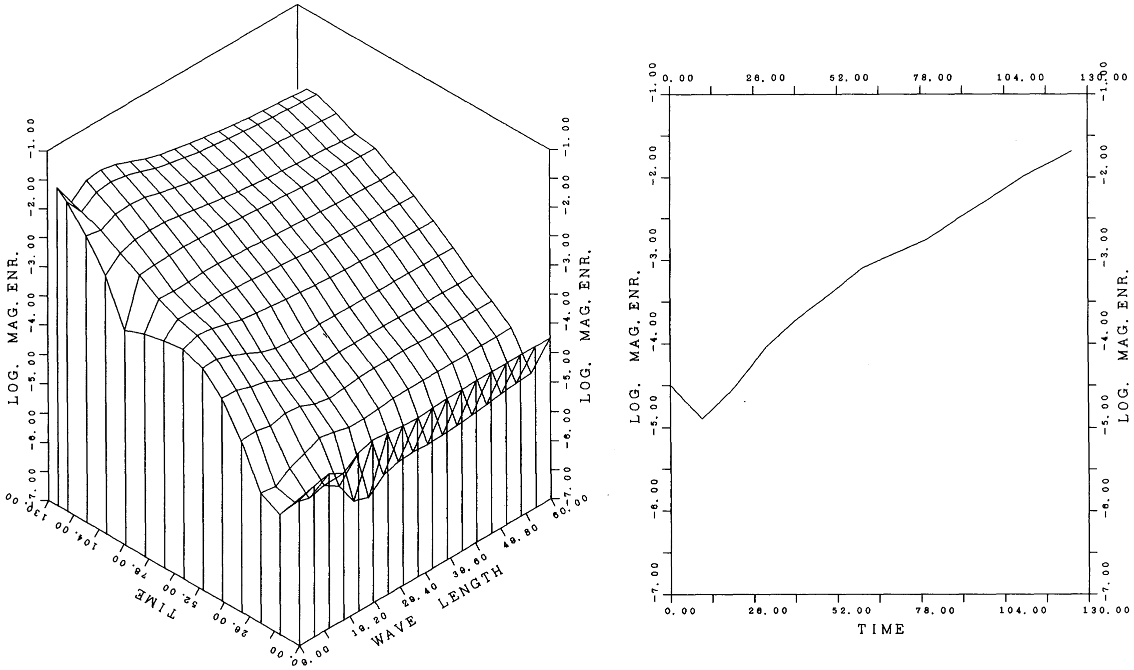

FIG. 6.—(*a*) Three-dimensional display of the time evolution of the logarithmic Fourier coefficients of the magnetic energy (defined by eq. [31]). (*b*) Time evolution of the logarithmic Fourier coefficient of the magnetic energy with $\lambda = 18\ R$, which shows the most rapid growth in (*a*). The growth rate is $\sim 0.06 V_j/R$.

4.2. *Relationship between Wiggles of Structure and Line-of-Sight Velocity*

We next focus our attention on the line-of-sight velocity for our calculated jet in order to compare it with the observed velocity distribution in the wiggled structure of the HH objects. In our MHD-unstable jet, the magnetic field controls the dynamics in the wiggled filament, as well as the growth of the helical deformation of the jet. When the instability saturates, the gas begins to flow along the helical structure, and v_ϕ becomes much larger than v_r. In the resulting flow along the helical structure, the line-of-sight velocity takes on its maximum or minimum value at the position where the sine-curve displacement in the plane of sky (which is actually a projection of a helical structure) takes on its maximum value. In contrast, in the case of a precessing source model, v_r is much larger than v_ϕ, which is exactly zero; the line-of-sight velocity then would take on its maximum or minimum value on the projected axis of the cone on which the helix lies. To summarize: if we compare the apparent sine-curve structure with the line-of-sight velocity measured along this structure, then the phase deviation between them is 0° or 180° for the helical flow case, but is 90° or 270° for the precessing source model.

In addition, the axial and azimuthal velocities and the helical structure have a particular relation in the case of the helically structured flow: consider the saturated stage of the instability ($v_\phi \gg v_r$), neglect the motion of the helical structure itself, and let us denote the displacement of the helical structure from its axis as a, and its pitch as L. If the velocity field is completely along the helical structure, we can relate the ratio of v_ϕ to v_z to the structure itself by simple geometry, e.g.,

$$\frac{v_\phi}{v_z} = \frac{2\pi a}{L} . \tag{36}$$

The obvious question is then whether the simulations show any evidence for this scaling. From our results in Figure 3, we can evaluate the left-hand side of equation (36) in the wiggles; we find that the ratio is $\sim$0.2–0.5. Similarly, we can evaluate the right-hand side, obtaining $\sim$0.3 ($a \sim 0.5\ R$ and $L \sim 10\ R$). This numerical coincidence is again consistent with our interpretation that the gas has begun to flow along the helical structure.

This relation can be further quantified with the use of available observational quantities. We denote the absolute value of the mean line-of-sight velocity of a wiggled part of a HH object by $v_{\rm mean}$, the amplitude of a fluctuation of the line-of-sight velocity by $v_{\rm fluc}$, the angle between the axis of the HH object and the observer by ψ, and the pitch of the wiggled part in the plane of the sky by $L_{\rm obs}$. If the observed wiggled structure of the HH object is in fact a helical structure, and if the gas does flow completely along this helical structure, then the observed line-of-sight velocity is

$$v_{\rm mean} = v_z \cos \psi , \tag{37}$$

$$v_{\rm fluc} = v_\phi \sin \psi . \tag{38}$$

From these equations, and upon making use of equation (36) and the relation $L_{\rm obs} = L \sin \psi$, we obtain the following relationship connecting the ratio of the fluctuating and mean line-of-sight velocity to the geometric characteristics of the structure:

$$\frac{v_{\rm fluc}}{v_{\rm mean}} = \frac{2\pi a}{L_{\rm obs}} \tan \psi \sin \psi . \tag{39}$$

Let us evaluate equation (39) for the wiggled filament of HH 46/47. The line-of-sight velocity in Plate 1.(a) of Meaburn & Dyson (1987) has two properties, one of which is that the mean line-of-sight velocity decreases (increases in its absolute value) from HH 46 towards HH 47A, an the other of which is an observed sine-curve-like fluctuation about the mean velocity. If we set $v_{\rm fluc}$ as a typical amplitude of the fluctuation, we find $v_{\rm fluc} \sim 15\ {\rm km\ s^{-1}}$ and $v_{\rm mean} \sim 160\ {\rm km\ s^{-1}}$. Thus, for HH 46/47, the left-hand side of equation (39) is $\sim$0.1. In order to evaluate the right-hand side, we refer to Figure 4.b of Reipurth & Heathcote (1991). We identify the length between knots A_{17} and B_{11} with $L_{\rm obs}$, and have $L_{\rm obs} = 40''$. We also adopt $a \sim 1''$ from that figure. Thus, if we set $\psi = 60°$ as a working value, the right-hand side of equation (39) is $\sim$0.2. For HH 46/47, the left-hand and right-hand sides of equation (39) coincide with one another within a factor of 2. This rough coincidence yet again suggests that the magnitude of the fluctuation of the line-of-sight velocity of the wiggled filament of HH 46/47 can be explained as a helical flow along the helical structure which is formed by a helical kink instability. Although the ratio of v_ϕ to v_z in the results of our simulation is somewhat larger (with a factor of 1–3) than $v_{\rm fluc}/v_{\rm mean}$ observed in the wiggled filament of HH 46/47, this ratio depends on the helical structure, which in turn is determined by the initial magnetic field in our model. We believe that more appropriate initial magnetic field (which has a lower ratio of B_ϕ to B_z than that adopted here) would result in a helical structure with a lower ratio of $2\pi a$ to L, and also in a lower v_ϕ/v_z. More discussion of this point will be given in a following paper.

4.3. *Effect of Flow Helicity on Kink Instability*

As mentioned in § 3.1, there are two spatial domains in which B_ϕ appears strong, which lie between the forward-propagating fast-mode shock and slow-mode shock, and between the backward-propagating fast-mode shock and slow-mode shock ("forward" and "backward" with respect to a coordinate system moving with the contact discontinuity).

It is interesting to note that the helical kink instability takes place only in the backward-propagating region, and it does not occur in the forward-propagating region. This difference is readily explained by appealing to the internal spinning motions already alluded to. H. Hamatake (1992, private communication) and G. Bodo (1992, private communication) have both performed linear analyses of the stability of a cylindrical helical flow of an infinite length with a helical magnetic field. Both found that a helical flow with the same sign of helicity as that of the helical magnetic field enhances the $m = 1$ instability, whereas a flow with the opposite sign of helicity reduces the instability growth rate. The result of our nonlinear simulation is thus consistent with the result of these linear analyses.

5. SUMMARY

We have adopted a model describing the physical circumstances prevailing in the vicinity of a forming star discussed by Uchida & Shibata (1985, 1986; Shibata & Uchida 1986), and have used it to carry out a three-dimensional MHD simulation of the dynamics of a jet interacting with an ambient large-scale magnetic field. In the earlier studies, it was shown that the twisting up of the large-scale magnetic field by the differentially rotating protostellar disk produces spinning bipolar flows, as well as angular momentum loss in the protostellar disk due to magnetic braking by the large-scale magnetic field. This resulted in an enhanced accretion rate onto the central forming star (Uchida & Shibata 1985, 1986; Shibata & Uchida 1986; Uchida et al. 1987a, b). In this model, the azimuthal component of the magnetic field is continuously created in the differentially rotating accretion disk, and propagates out along the large-scale magnetic field; as it does so, it pinches the ambient medium and the poloidal magnetic field toward the symmetry axis, thus changing the morphology of the large-scale magnetic field from that of an hour-glass type configuration to that of a rodlike configuration in which the internal field is helical. Both the poloidal and toroidal components of the magnetic field will thus be enhanced over those of the background magnetic field in the interstellar medium. We assume that YSO jets are then ejected from the forming star along the polar axis (Uchida & Shibata 1984; Hirose et al. 1993) under such circumstances.

We have performed three-dimensional MHD simulations of a YSO jet under such circumstances. We find that four shocks are formed, namely (enumerating from the farthest shock) a fast-mode shock, a slow-mode shock, a slow-mode shock, and a fast-mode shock; the former two propagate forward, while the latter two propagate backward in the coordinate moving with the contact discontinuity.

The jet which propagates in this manner is unstable to the helical kink instability due to the toroidal magnetic field component (B_ϕ); the strength of this field component in the initial state is $\sim 70\ \mu$G (within the jet), with a jet density of 100 $m_{\rm H}$ cm^{-3} and a jet velocity of 100 km s^{-1}. This instability is primarily localized between the backward-propagating fast-mode shock and the backward-propagating slow-mode shock.

Shock compression and a helical flow of the same helicity as the magnetic field both enhance the helical kink instability. We show that the ($-j_z B_\phi$) force acts to drive the instability and that the helical magnetic field reduces its internal twist by transferring its helicity to larger scales. We have compared our results with that of the sheath current approximation, confirming that they are consistent.

The toroidal velocity component between the forward-propagating fast-mode shock and the forward-propagating slow-mode shock is a consequence of internal spinning motions within the filament; in contrast, the same velocity component is seen in the region where the helical kink instability has grown and is due to the flow along the flux tube which has been globally deformed into a large-scale helix. The latter helical flow shows a distinctly different character from the ballistic motion from the source in the precessing model of the wiggled structure.

To conclude, we have amassed a number of arguments showing the similarity between the results of our simulations and the observed characteristics of HH 46/47. Taken as a whole, our results therefore suggest strongly that the wiggled filament of HH 46/47 can be interpreted to have been formed by the helical kink instability.

The authors would like to thank Dr. K. Shibata for helpful discussions. This work was supported in part by the JSPS/NSF Japan-US Cooperative Science Program (Principal Investigators: Y. U. and R. R.) Numerical calculations were performed on the HITAC S820/80 at the Computer Center of the University of Tokyo, and the Fujitsu VP-200E at National Institute for Fusion Science.

REFERENCES

Böhm, K. H. 1989, in IAU Colloq. 120, Structure and Dynamics of the Interstellar Medium, ed. G. Tenorio-Tagle, M. Moles, & J. Melnick (Berlin: Springer-Verlag), 282
Brio, M., & Wu, C. C. 1988, J. Comp. Phys., 75, 400
Cantó, J. 1980, A&A, 86, 327
Clarke, D. A., Norman, M. L., & Burns, J. O. 1986, ApJ, 311, L63
Dyson, J. 1984, Ap&SS, 106, 181
Graham, J. A., & Elias, J. H. 1983, ApJ, 272, 615
Hirose, S., Uchida, Y., Shibata, K., Matsumoto, R., & Sato, T. 1993, in preparation
Kössl, D., Müller, E., & Hillebrandt, W. 1990, A&A, 229, 378
Kruskal, M. D., Johnson, J. L., Gottlieb, M. B., & Goldman, L. M. 1958, Phys. Fluids, 1, 421
Lind, K. R., Payne, D. G., Meier, D. L., & Blandford, R. G. 1989, ApJ, 344, 89
Low, B. C. 1984, ApJ, 281, 381
Meaburn, J., & Dyson, J. E. 1987, MNRAS, 225, 863
Mestel, L. 1965, QJRAS, 6, 161
Mouschovias, T. Ch., & Paleologou, E. V. 1979, ApJ, 230, 204
Mundt, R. 1985, in Protostars and Planets II, ed. D. Black & M. Matthews (Tucson: Univ. of Arizona Press), 414
Mundt, R., Brugel, E. W., & Bührke, T. 1987, ApJ, 319, 275
Mundt, R., & Fried, J. W. 1983, ApJ, 274, L83
Norman, C., & Silk, J. 1979, ApJ, 228, 197
Norman, M. L., Smarr, L., Winkler, K.-H. A., & Smith, M. D. 1982, A&A, 113, 285
Raga, A. C. 1989, in Proc. ESO Conf. & Workshop, Low-Mass Star Formation and Pre–Main-Sequence Objects, ed. B. Reipurth (Garching: ESO), 281
Reipurth, B. 1989, in Proc. ESO Conf. & Workshop, Low-Mass Star Formation and Pre–Main-Sequence Objects, ed. B. Reipurth (Garching: ESO), 247
Reipurth, B., & Heathcote, S. 1991, A&A, 246, 511
Roe, P. L. 1981, J. Comput. Phys., 43, 357
Schwartz, R. D. 1975, ApJ, 195, 631
———. 1978, ApJ, 223, 884
Shafranov, V. D. 1957, Soviet Phys.—JETP, 6, 545
Shibata, K., & Uchida, Y. 1986, PASJ, 38, 631
Strom, K. M., Strom, S. E., & Stocke, J. 1983, ApJ, 271, L23
Strom, K. M., Strom, S. E., Wolff, S. C., Morgan, J., & Wenz, M. 1986, ApJS, 62, 39
Todo, Y. 1991, Ph.D. thesis, University of Tokyo
Todo, Y., Uchida, Y., Sato, T., & Rosner, R. 1992, PASJ, 44, 245
Uchida, Y., Kaifu, N., Shibata, K., Hayashi, S. S., & Hasegawa, T. 1987a, in Star-forming Regions, ed. E. Peimbert & J. Jugaku (Dordrecht: Reidel), 285
Uchida, Y., Kaifu, N., Shibata, K., Hayashi, S. S., Hasegawa, T., & Hamatake, H. 1987b, PASJ, 39, 907
Uchida, Y., & Shibata, K. 1984, PASJ, 36, 105
———. 1985, PASJ, 37, 515
———. 1986, Canadian J. Phys., 64, 507
Uchida, Y., Todo, Y., Rosner, R., & Shibata, K. 1992, PASJ, 44, 227
van Leer, B. 1979, J. Comp. Phys., 32, 101